CHEMISTRY OF MATERIALS

pubs.acs.org/cm

Article

# Enriching Unsaturated Coordination for High-Performance Chromium Oxide Catalysts

Mingxin Lv, Qiang Li,* Fan Xue, Zhiguo Li, Peixi Zhang, Longlong Fan, Jianrong Zeng, Mengshi Li, Yufei He, Dianqing Li, Qiheng Li, Xin Chen, Kun Lin, Jinxia Deng, and Xianran Xing

Cite This: https://doi.org/10.1021/acs.chemmater.4c02260

Read Online

ACCESS | Metrics & More | Article Recommendations | Supporting Information

**ABSTRACT:** Chromium oxide catalysts are a type of industrial catalyst that is commonly utilized in heterogeneous catalytic processes. Their outstanding catalytic activity is accomplished through the efficient interception of unsaturated coordination and favored surface aggregation. However, the increase of surficial unsaturated coordination and its structural characterization continues to challenge the limitations of chemical synthesis and atomic decoding of nanocatalysts. In this study, a thermal shock method was employed to intercept a significant number of unsaturated coordination and high-valence chromium species in $CrO_x$-based nanocatalysts. The transformation of nearest-neighbor symmetry from octahedral to tetrahedral was discovered to be centered on the surface of the nanoparticle through the atomic recognition of chromium species using the pair distribution function (PDF) and reverse Monte Carlo (RMC). The catalytic efficacy of symbolic catalytic reactions, such as the dehydrogenation of propane, toluene oxidation, and benzyl alcohol oxidation, is enhanced by the precise synthesis of the surficial active sites. Our results demonstrate a convenient chemical synthesis method that preserves the metastable structure of oxide catalysts under thermal shock. The atomic structural understanding also offers an intuitional experimental model for the study of reaction mechanisms.

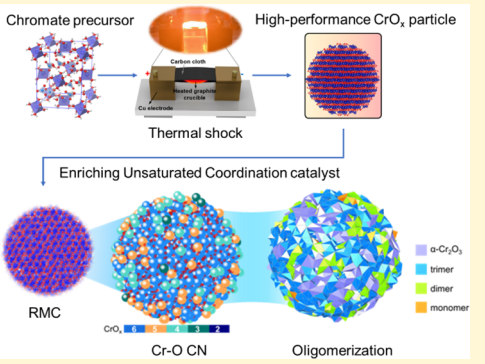




## INTRODUCTION

Defective oxides possess numerous active sites with diverse valence states, which are determined by the surrounding coordination environment. This characteristic has sparked a great deal of interest in studying their role in heterogeneous catalysis.[1] Chromium oxide ($CrO_x$) is extensively used in several industrial catalytic reactions, such as low-carbon alkane dehydrogenation,[2] ethylene polymerization,[3] and oxidation of volatile organic compounds (VOCs).[4] Due to the excellent C−H bond activation and $O_2$ adsorption capacity of the unsaturated coordination of $Cr^{3+}$, it is usually considered the active site in these reactions.[5,6] Hence, in the synthesis process of $CrO_x$-based catalysts, it is crucial to generate more defective structures and achieve a preferred surficial distribution.[7] This serves as the foundation for designing $CrO_x$-based catalysts and tailoring their hypotoxicity, which also provides important guidance for other oxide catalysts.

For the chromium oxide catalysts, the $\alpha$-$Cr_2O_3$ structure, belonging to the $R\bar{3}c$ space group,[8] is the stable structure at ambient temperatures and normal pressure. It consists of an organized arrangement of $CrO_6$ octahedra but often is not catalytically active in most catalytic reactions. The potentially active structures are the chromium species with a lack of coordination, which are usually observed in metastable compounds, $CrO_3$ or dichromate.[9] There are two main impediments to the intelligent development of $CrO_x$-based catalysts. The first issue is the scarcity of a proper method to enhance the fraction of defective structures on the surface of catalysts during chemical synthesis. The stabilization of structurally flawed catalysts and achieving technical universality are the primary challenges in the efficient preparation of catalysts. They raise the research popularity of chemical restraints based on the surface/interface strain,[10,11] structural induction of heterogeneous doping,[12,13] and postphysical/chemical processing.[14] In general, one of the solutions is the creation of ultrafine crystalline nanocatalysts. The abundant specific surfaces provide a platform for immobilizing the unsaturated species, while the structured frameworks enhance the stability of the service under operational conditions compared to that of the amorphous counterparts. Regrettably, it also triggers a conflict between the reduction in size to the nanoscale and the process of heat crystallization during the synthesis. Recently, thermal shock has become an effective method for synthesizing ultrafine nanoparticles and stabilizing abundant defects.[15] The use of the ultrafast heating/cooling

Received: August 12, 2024
Revised: December 9, 2024
Accepted: December 9, 2024

rate can lead to a variety of ultrafine and uniform bimetallic nanoparticles like CuSn, CuAg, CuPd, etc.,[16] and multiple defects like crystal twins will be stabilized in nanoparticles.[17] Through the careful adjustment of temperature and time of the thermal pulse, highly defective coordination can be obtained in ultrafine nanocatalysts.

The lack of structural decoding for the atomic three-dimensional model of $CrO_x$-based catalysts is another significant issue. The comprehension of the active sites of $CrO_x$-based catalysts is hindered by the intricate and varied chromium coordination within the oligomeric chromium species.[18,19] The primary challenge in locating active sites in nanocatalysts is the spatial differentiation that occurs from the surface to the core component. Conventional spectroscopic techniques, such as UV−vis spectra,[20,21] EPR,[22] and Raman,[23] can only determine the presence or absence of high-valence species, as well as the defective symmetry. However, the involvement of $CrO_x$ nanocatalysts in catalytic reactions is in the process of surface determination. The selectivity and activity are intricately linked to the outermost structure.[24] At the local scale, electron microscopy techniques are unable to differentiate the atomic defective structure of ultrafine nanoparticles. Hence, the precise identification of three-dimensional space and efficient arrangement of active sites continue to be the primary constraint for the targeted design and understanding of reaction mechanisms for $CrO_x$ nanocatalysts.

In this study, we utilized thermal shock synthesis to successfully achieve the efficient interception of defective Cr−O coordination in 4 nm crystalline $CrO_x$ nanocatalysts. By utilizing extensive spectroscopic approaches, we verified the generation of high-valence chromium species and the change of local coordination symmetry. This can increase the conversion rate of reactants about 50% in propane dehydrogenation and toluene and benzyl alcohol oxidation reactions. In order to obtain the real-space identification of the defective chromium, we employed reverse Monte Carlo (RMC) simulation for pair distribution function (PDF) to rebuild the atomic three-dimensional structure of $CrO_x$ nanocatalysts. The accurate identification of chromium coordination and its aggregation confirmed the successful capture of unsaturated chromium species and oligomers. Our research offers a handy approach to acquire defective nanocatalysts and achieve exact atomic elucidation of the structural foundation of high-performance catalysts.

## EXPERIMENTAL SECTION

**Catalyst Preparation.** 0.5264, 0.7897, and 1.0529 g of chromium(III) nitrate nonahydrate ($Cr(NO_3)_3{\cdot}9H_2O$, 99%) were dissolved in 30 mL of deionized water. Then, 1 g of silica gel was added, stirred at 80 °C for 3 h, and dried at 95 °C for 12 h to obtain the precursor. 50 mg of precursor was placed into a graphite crucible and clamped between the carbon cloth. The size of the carbon cloth was 1.6 × 15 cm, and the diameter of the graphite crucible was 1.5 cm. The thermal shock heating was conducted under air conditions by using a DC power supply with an output voltage of up to 30 V and an output current of up to 40 A. 1100 °C thermal shock treatment was performed to synthesize 10, 15, and 20 wt % $CrO_x/SiO_2$-TS catalysts. The time for each cycle was about 4 s, and the heating time in the cycle was around 0.55 s. The 20 wt %-C catalyst was obtained by calcining 500 mg of precursor at 700 °C for 6 h.

**Characterization.** The powder X-ray diffraction (XRD) patterns were measured on a PANalytical X'pert PPR diffractometer with Cu K$\alpha$ radiation ($\lambda$ = 1.54 Å, 40 kV, and 30 mA), and a scanning angle of 20°−70°. The total Cr content in the catalysts was determined by ICP spectrometry (PerkinElmer ICP 2100). X-ray photoelectron spectra were measured on a Thermo Scientific K-Alpha. Charge correction was used with the C 1s orbital binding energy, and Cr 2p spectra were analyzed by using XPSPEAK software. The UV-3600 equipped with an integrating sphere was used to collect UV−vis data, using $BaSO_4$ as a blank backing, and the testing range was 200−800 nm. EPR spectra were recorded on a Bruker EMXplus-6/1 spectrometer (X-band, $\nu \approx$ 9.8 GHz) with a microwave power of 2 mW, a modulation frequency of 100 kHz, and a modulation amplitude of 4 G. HR-TEM data were collected by a Titan ETEM G2 at 80 kV. The temperature-programmed reduction of $H_2$ was conducted on an AutoChem1 II 2920 with a thermal conductivity detector. Before testing, the catalysts (approximately 100 mg) were swept with high-purity Ar gas at 300 °C for 1 h and cooled to 50 °C to remove water or impurities. Then, the temperature was increased from 50 to 700 °C at a rate of 10 °C/min under 30 mL/min of 10% $H_2$/Ar. Nitrogen adsorption−desorption isotherms were measured at 77 K using ASAP2460, and the samples were degassed at 250 °C for 6 h before measurements. Thermogravimetric analysis (TG) and differential scanning calorimetry (DSC) were performed on a PerkinElmer STA 8000. The samples were heated in a flux of air (20 mL/min). The temperature range was 50−700 °C, and the heating rate was 10 °C/min.

XAFS spectra were collected at the Cr K-edge on the BL13SSW beamline of the Shanghai Synchrotron Radiation Facility in transmission mode at room temperature. The Demeter package was used to fit the data.[25] Wavelet transform (WT) of EXAFS was implemented by using the HAMA software.[26] The atomic pair distribution function (PDF) was obtained from the 3W1 beamline at the Beijing Synchrotron Radiation Facility with a wavelength of 0.2061 Å and the BL13SSW beamline at the Shanghai Synchrotron Radiation Facility with a wavelength of 0.2072 Å by direct Fourier transform of the reduced structure function with a Q value of 18 $Å^{-1}$ by PDFgetX2 software.[27] Small box fitting was carried out on PDFgui based on the $Cr_2O_3$ (R-3C) phase. The RMC profile was used for Reverse Monte Carlo simulation of the PDF data in big box fitting, based on the small box fitting unit cell, expanding this unit cell to a sphere with a radius of 20 Å and placing it in a 100 Å × 100 Å × 100 Å vacuum box to generate the initial model of RMC. DISCUS was used to analyze the atomic spatial distribution and atom local coordination environment based on the model from RMC.[28] The Cr−O coordination number was extracted by counting the number of O atoms in the 0−2.5 Å range around chromium atoms. The species of oligomerization was distinguished by counting the number of Cr atoms in the 0−3.2 Å range around chromium atoms.

**Catalytic Activity Tests.** Toluene oxidation tests were carried out by adding 0.3 mL of toluene, 10 mL of acetonitrile, 50 mg of $CrO_x/SiO_2$ catalyst, and 20 mg of NaBr to a three-necked flask with a condenser tube. 6 mL of hydrogen peroxide was added slowly over 1 h after the temperature had increased to 90 °C. The reaction was stopped after continuing for 2 h. The products were analyzed online by a Shimadzu GC-2010 equipped with a flame ionization detector.

Benzyl alcohol oxidation tests were carried out by adding 0.3 mL of benzyl alcohol, 10 mL of acetonitrile, and 50 mg of $CrO_x/SiO_2$ catalyst to a three-necked flask. The reaction temperature was 110 °C, oxygen was used as the oxidant, and the reaction system pressure was maintained at 0.1 MPa. The reaction was stopped after six hours. The products were analyzed online by a Shimadzu GC-2010 equipped with a flame ionization detector.

Propane dehydrogenation tests were carried out in a fixed-bed reactor with a loading amount of 100 mg. The catalyst was packed into a steel pipe with an inner diameter of 7.5 mm. Before the reaction, the catalyst was heated at 560 °C at a rate of 10 °C /min and pretreated with nitrogen gas for 30 min. The $N_2$ gas flow rate was 50 mL/min. Afterward, the catalyst was evaluated at 560 °C. The gas composition of the reaction gas was $C_3H_8$:$N_2$ = 1:9, with a flow rate of 20 mL/min and a reaction atmospheric pressure of 1 atm. Catalyst regeneration was performed with 50 mL/min of air for 60 min. After regeneration, the catalyst was purged with $N_2$ at 50 mL/min for 30 min. The products were analyzed online by a Techcomp GC7980


https://doi.org/10.1021/acs.chemmater.4c02260
Chem. Mater. XXXX, XXX, XXX−XXX

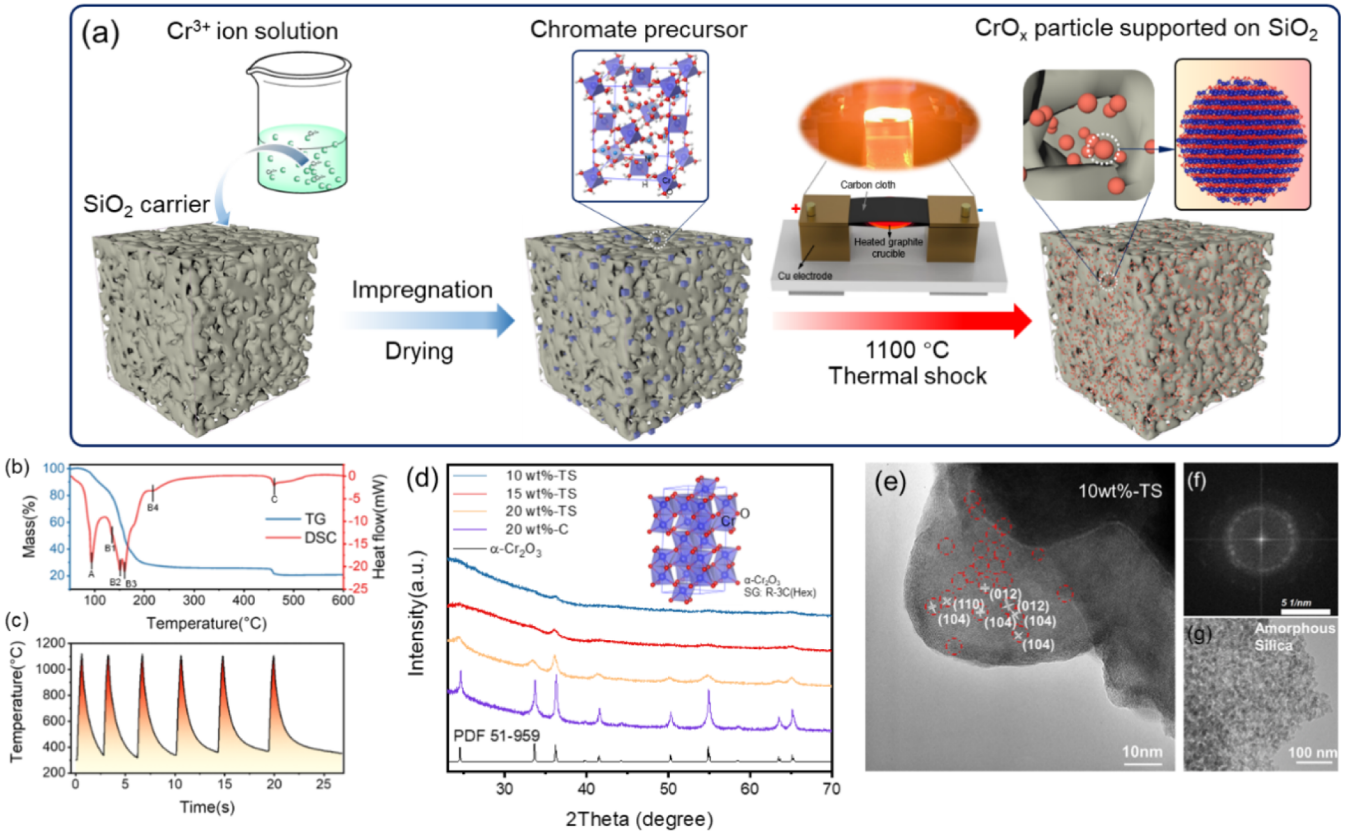


**Figure 1.** (a) The schematic illustration of the synthesis of defective $CrO_x$ nanocatalysts by thermal shock. (b) TG-DSC curves of chromium (III) nitrate nonahydrate. (c) Thermal pulses detected during the synthesis. (d) X-ray powder diffraction patterns of 10 wt %, 15 wt %, and 20 wt %-loading samples by thermal shock (TS), and the 20 wt %-loading sample by calcining. (e,f) HRTEM and FT images for 10 wt %-TS. (g) TEM image of amorphous silica.

equipped with a flame ionization detector. The equations for catalyst performance are shown in the Supporting Information.

## RESULT AND DISCUSSION

**Synthesis of the High-Unsaturated $CrO_x$ Nanocatalyst.** The precursor chosen to be loaded onto the silica gel was chromium (III) nitrate nonahydrate, as indicated in Figure 1a. Next, it was evenly placed on the graphite crucible in order to undergo Joule thermal shock using direct current. Chromium (III) nitrate dihydrate exhibits a fully octahedral coordination around the $Cr^{3+}$ cations. The TG-DSC curves (Figure 1b) illustrate three distinct stages of chemical decomposition or conversion of chromium (III) nitrate nonahydrate. Stage A represents the partial disintegration of lattice water, whereas the main loss of mass happens in stage B. After that, the high-valence solid product as $Cr_4O_8$ will be generated, which undergoes a transformation to $Cr_2O_3$ at a temperature of 450 °C.[29] The decomposition process of the precursor demonstrates the interception possibility of high-valence chromium oxide. To assess the necessary level of crystallinity for $CrO_x$-based nanocatalysts, six thermal pulses at 1100 °C were applied to the precursor with different loading capacities, marked as 10, 15, and 20 wt %-TS (Figure 1c). Compared with the calcined sample at 700 °C, marked as 20 wt %-C, samples synthesized by thermal shock have a broader peak width indicating smaller particle size (Figure 1d), and the diffraction peaks of these samples are at lower angles (Figure S4), suggesting that the samples synthesized by thermal shock have larger single-cell parameters. The X-ray diffraction patterns show that all samples can be indexed as the $\alpha$-$Cr_2O_3$ phase. In the HRTEM and FT images of 10 wt %-TS, the ordered fringe indicates a nanosize of about 4 nm which contributes to the consistent diffraction rings as the $\alpha$-$Cr_2O_3$ phase on the surface of amorphous silica (Figure 1e–g). As loading rises to 20%, the size of 20 wt %-TS will increase to about 5 nm (Figure S1), and the size of the calcined sample is above 150 nm (Figure S2). The statistical analyses of the catalyst size synthesized by thermal shock are shown in Figure S3.

The BET surface area, pore diameter, and true loading of catalysts were obtained from $N_2$ adsorption isotherms and ICP spectrometry and are shown in Table S1. As the loading rises, the BET area of fresh catalysts gradually decreased from 479.6 to 441.7 $m^2/g$, and the BET area of the silica support is 531.6 $m^2/g$. Combined with the fact that the pore diameters of the catalysts are all about 5.7 nm, this suggests that the high-temperature treatment did not change the surface structure of the silica. Further, by comparing the spent 10 wt %-TS catalyst with the fresh catalysts, their BET areas and pore diameters were not significantly different, indicating that the structure of the silica was also not significantly changed during the reaction. The ICP results proved the existence of Cr evaporation during the synthesis of the catalysts, and the process of thermal shock synthesis will evaporate a bit more.

The UV–vis spectra will exhibit changes in unsaturated coordination and symmetry due to the sensitivity of the electronic structure to defect generation in chromium-related compounds. Figure 2a clearly demonstrates that the sample 20 wt %-C exhibits a distinct and strong band at wavelengths of


https://doi.org/10.1021/acs.chemmater.4c02260
Chem. Mater. XXXX, XXX, XXX−XXX

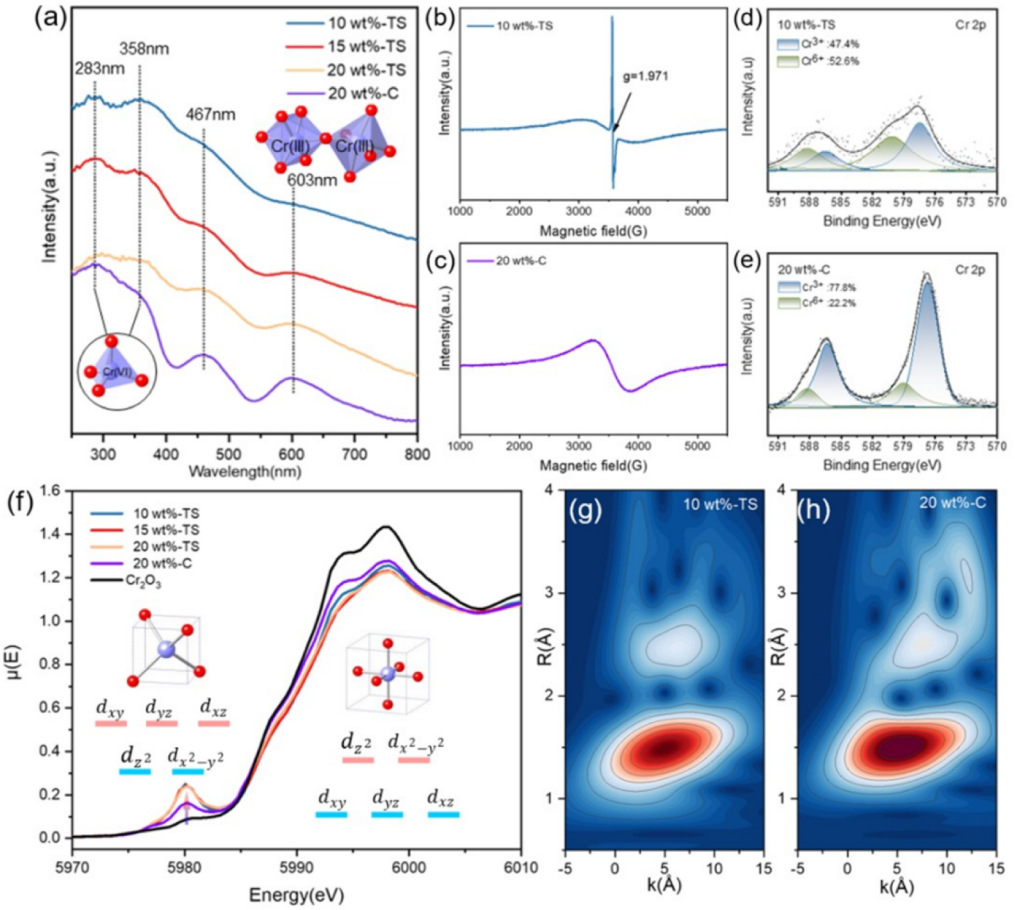


**Figure 2.** (a) UV−vis spectra of the synthesized $CrO_x$-based nanocatalysts. (b,c) Electron paramagnetic resonance (EPR) spectra of 10 wt %-TS and 20 wt %-C. (d,e) X-ray photoelectron spectra (XPS) of Cr-2p for 10 wt %-TS and 20 wt %-C. (f) X-ray absorption near edge structure (XANES) of the Cr K-edge for the synthesized $CrO_x$-based nanocatalysts and bulk $Cr_2O_3$. (g,h) Wavelet transform of EXAFS for 10 wt %-TS and 20 wt %-C.

603 nm and 467 nm. This band corresponds to the $T_{2g}\leftarrow A_{2g}$ and $T_{1g}\leftarrow A_{2g}$ transitions in the octahedral symmetry.[30,31] Comparatively, the samples prepared by thermal shock exhibit the suppression feature for this band. Simultaneously, the bands at 283 nm and 358 nm were highlighted, indicating the O→Cr(VI) charge transfer of the $^1T_2\leftarrow{}^1A_1$ type in the tetrahedral chromate.[32] The bands in the UV−vis spectra exhibit continuous changes from the unsaturated coordination, such as the tetrahedral symmetry, in the $\alpha$-$Cr_2O_3$ lattice. These changes are generated through the long-range averaging of defective octahedra-linked structures, which are formed using thermal shock. The loss of coordination will induce the unpaired electron and alter the spatial arrangement around Cr, resulting in a new resonance signal in EPR.[33] Figure 2b,c demonstrates that the calcined sample only exhibits a broad signal corresponding to the $\beta$-signal of $Cr_2O_3$-like clusters, which responds to the octahedral structure. However, a new peak at $g$ = 1.971 is observable in the sample from thermal shock as 10 wt %-TS. This means a different Cr species is generated, and the square pyramidal coordination is commonly referred to this signal,[34] as a result of the unsaturated conversion of the $CrO_6$ octahedron. Identical signals are also observed in other samples synthesized by thermal shock (Figure S5), proving that the thermal shock method is favorable for producing unsaturated coordination structures. The XPS spectra of Cr 2p are shown in Figure 2d,e, where two oxidation states of Cr ions can be detected. The peak around 580.1 eV is assigned to $Cr^{6+}$ and the peak at about 577.2 eV is attributed to $Cr^{3+}$ species.[35] Compared with 20 wt %-C catalyst, 10, 15, and 20 wt %-TS (Figure S6) catalysts all have higher peaks of $Cr^{6+}$, which might mean that the valence state of Cr ions will move higher as the concentration of unsaturated coordination structures increases. Catalysts' reducibility is recognized by $H_2$-TPR (Figure S7), and the catalysts synthesized by thermal shock consume more hydrogen, meaning they have more high valence Cr ions and reducible chromic sites. The peak area at 300−380 °C of the 10 wt %-TS catalyst has the highest proportion, and this peak area corresponds to the Cr sites considered as the precursors' active sites for catalysis.[40] As a result of the fundamental frameworks of the $\alpha$-$Cr_2O_3$ lattice, the average valence of chromium ions, which is determined by the maximum slope of XANES curves (Figure 2f), remains nearly unchanged compared to the bulk $\alpha$-$Cr_2O_3$ phase. However, the growing strength of the pre-peak indicates the presence of more vacant d orbitals of chromium, suggesting a higher valence of partial chromium ions.[36,37] However, the differentiation between unsaturated coordination or nearby symmetry changes is invisible in EXAFS (Figure S8). The fittings for the coordination shells of neighboring atoms (Figure S9 and Table S2) exhibit similar coordination counts and bond lengths. The wavelet transforms just indicate the subtle


https://doi.org/10.1021/acs.chemmater.4c02260
Chem. Mater. XXXX, XXX, XXX−XXX

modification of the lattice structure in the thermal-shock sample, as seen by the decrease in peak intensity (Figures 2g,h and S10).

**Evaluation of Catalytic Performance.** By subjecting $CrO_x$ nanocatalysts to thermal shock, it is possible to enhance their catalytic performance by addressing the issues of defect structures and unsaturated coordination. For the purpose of evaluating the catalyst's performance, we have selected three coordination-sensitive reactions: direct dehydrogenation of propane, catalytic oxidation of toluene, and catalytic oxidation of benzyl alcohol. For direct dehydrogenation of propane, Figure 3a demonstrates that the catalysts produced by the

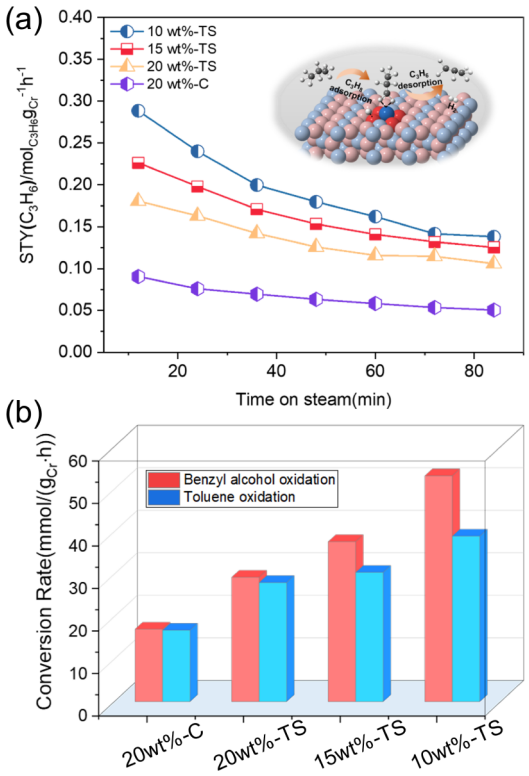


**Figure 3.** (a) Time on-stream for the propylene time space yield for the synthesized $CrO_x$-based catalysts. (b) Conversion rate of benzyl alcohol and toluene in the catalytic oxidation reaction for the synthesized $CrO_x$-based catalysts.

thermal shock method exhibit a significant increase in the time space yield. At 560 °C and a WHSV of 1.88 $h^{-1}$ conditions, the time space yield of 10 wt %-TS is 0.289 $mol_{C3H6}{\cdot}g_{Cr}{}^{-1}{\cdot}h^{-1}$, which is twice as much as 20 wt %-C. Meanwhile, the thermal-shock nanocatalyst also has 95% propylene selectivity, which is 5% higher than the 20 wt %-C catalyst (Figure S11). Besides, thermal-shock nanocatalysts can maintain high activity and selectivity at the same time at low temperature and high airspeed conditions compared with chromium-based catalysts (Figure S12). For catalytic oxidation of toluene and benzyl alcohol, Figure 3b demonstrates that using the 20 wt %-C catalyst, only about 20 mmol toluene or benzyl alcohol will convert in one hour. However, when thermal-shock nanocatalysts, with the same Cr element usage, toluene and benzyl alcohol would have over twice the conversion rate, and toluene or benzyl alcohol are more inclined to convert to benzaldehyde and benzoic acid. This is related to their high catalytic activity (Figure S13). The performance evaluation has shown that a significant number of unsaturated coordination sites resulting from the thermal shock approach contribute to the facilitation of the $CrO_x$-related catalytic process.

Furthermore, the weight loss behavior of spent catalysts was tested under an oxygen atmosphere at 150−700 °C to characterize the changes of deposit content (Figure S14). Catalysts synthesized by thermal shock have a higher amount of carbon deposition in the same reaction time, even though they have higher selectivity for propylene, which is considered to result from the fact that they are catalyzing more propane. The cycling of the 10 wt %-TS catalyst was also evaluated (Figure S15). The initial activity of the catalyst started to stabilize after a 13% decline in the first cycle, and the initial activity after cycles was also significantly higher than 20 wt %-C.

The catalytic activity of the catalysts calcined at 700 °C with 3 wt % loading and 1100 °C with 20 wt % loading for the propane dehydrogenation reaction was also characterized. As the loading of the catalysts synthesized by calcination is decreased, the activity of the catalyst improves to 0.1867 $mol_{C3H6}g_{Cr}{}^{-1}h^{-1}$, but it is not as high as the samples synthesized by thermal shock (Figure S17). However, when the calcination temperature of the catalyst was raised to 1100 °C, the conversion rate of propane decreased to about 1%, with almost no catalytic activity (Figure S18).

**Atomic Three-Dimensional Decoding of Unsaturated Coordination.** The spectroscopic results provided a thorough analysis and confirmed the effectiveness of the thermal shock approach in enhancing the catalytic performance of unsaturated coordination. Nevertheless, the primary locations for catalytic reactions predominantly occur on the surfaces of nanocatalysts.[38] The presence of structural characteristics that contribute to exceptional catalytic performance does not directly offer a conclusive model for understanding the reaction mechanism.[39] The precise determination of the three-dimensional arrangement of structural defects at the atomic level is crucial in understanding the exceptional performance of thermal-shock $CrO_x$ nanocatalysts. Here, we employed the pair distribution function (PDF) to differentiate the structural characteristics of atomic pairs at varying distances and their correlation.[40,41] Figure 4a demonstrates that the PDFs of the samples obtained by using thermal shock and calcining both display the primary feature of the $\alpha$-$Cr_2O_3$ lattice. However, there are noticeable variations in several neighboring pairs within the 4 Å range. By utilizing the $\alpha$-$Cr_2O_3$ phase, it is possible to do real-space fitting of the PDF within a range of 20 Å (Figure S16).

This analysis reveals a clear deviation in the closest Cr−O bonds and the first two Cr−Cr pairs. In the pure $\alpha$-$Cr_2O_3$ phase, the $CrO_6$ octahedral coordination results in Cr−O bonds with identical lengths of approximately 1.95−2.05 Å.[42] The presence of short Cr−O bonds with lengths ranging from 1.55 to 1.75 Å indicates the occurrence of local tetragonal coordination.[43] The $\alpha$-$Cr_2O_3$ phase consists of honeycomb layers composed of octahedra that share edges. These layers stack along the *c*-axis, with alternating slips in opposing directions perpendicular to the *b*-axis (see Figure 4b). This process of disassembling the structure allows for the extraction of the unit oligomer consisting of 3 octahedra. It is formed through the in-layer edge-sharing connection, interlayer plane-sharing link, and diagonally corner-sharing link (refer to the inset in Figure 4a). Correspondingly, the presence of several Cr−Cr bonds measuring 2.89 Å, 2.65 Å, and 3.65 Å is


https://doi.org/10.1021/acs.chemmater.4c02260
Chem. Mater. XXXX, XXX, XXX−XXX

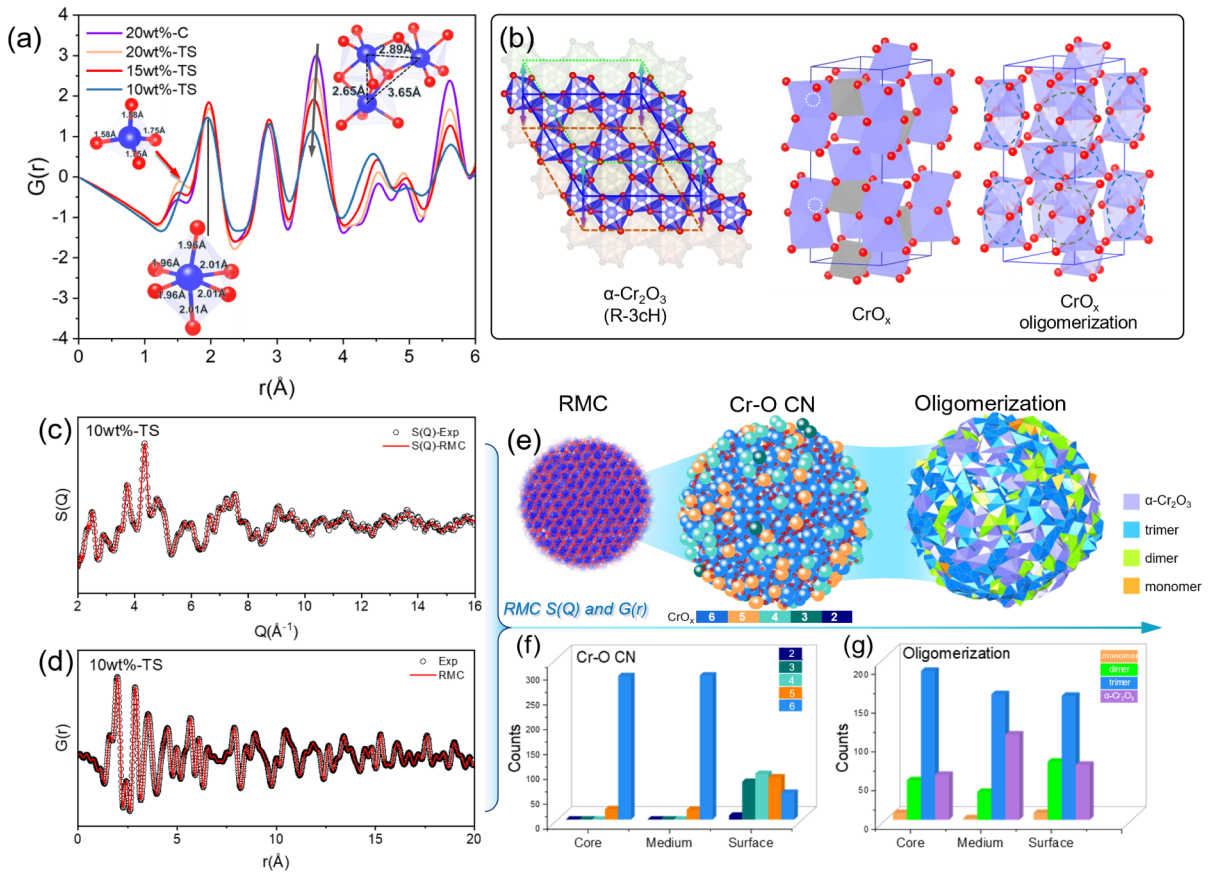


**Figure 4.** (a) Pair distribution function (PDF) of synthesized $CrO_x$-based nanocatalysts. The insets show the nearest-neighbor coordination and bond length of octahedral and tetrahedral chromium species. (b) Structure of $\alpha$-$Cr_2O_3$, the defective Cr octahedra, and oligomerization. (c,d) Reverse Monte Carlo (RMC) simulation for the PDF of 10 wt %-TS combined with $S(Q)$ and $G(r)$. (e) Atomic model from RMC and the extraction of the spatial distribution of the coordination number and oligomerization. (f,g) Statistics according to the shell of the nanocatalyst. The shell thickness is 3.5 Å for surface and medium shells.

observed. The application of the thermal shock method and the decrease in loading capacity resulted in a reduction of the Cr−Cr pair by approximately 3.65 Å, indicating the loss of the corner-sharing connection. As a result, the original $\alpha$-$Cr_2O_3$ lattice was divided into smaller groups of dimers or trimers. To determine the spatial arrangement of unsaturated coordination in the $CrO_x$-nanocatalysts, we performed reverse Monte Carlo (RMC) simulations on the $S(Q)$ and $G(r)$ of 10 wt %-TS (Figure 4c,d). The atomic model was analyzed to determine the nearby coordination. Figure 4e reveals an abundance of unsaturated coordination, such as $CrO_5$ and $CrO_4$, present on the outermost surface. These defective coordinations account for 83% of the surface section in the RMC model. In contrast, they only accounted for 7% of the core section. Alternatively, the polymerization of chromium species can be retrieved based on the proximity of coordination numbers between Cr−Cr pairs (Figure 4g). The spatial distribution characteristics of the defective coordination and polymerization of chromium species were compared. The surface of $CrO_x$ nanocatalysts from thermal shock results in the formation of defective oligomers such as dimers or trimers. These oligomers have a higher valence than the $Cr_2O_3$-like clusters known as "Soft Cr(VI)".[44] Compared with $CrO_6$, the unsaturated coordinated Cr sites like $CrO_5$ or $CrO_4$ in them are more prone to adsorb reactant molecules like $C_3H_8$ or $O_2$, and activate C−H bonds to generate intermediates, ultimately accelerating the rate of product generation.[45,46] This precise distribution of unsaturated coordination enables the formation of easily reducible active sites, hence enhancing defect-related catalytic activities.

## CONCLUSION

In conclusion, the thermal shock approach has successfully generated a significant quantity of unsaturated coordination structures in $CrO_x$-based nanocatalysts. The change in coordination symmetry from octahedral to tetrahedral resulted in the formation of high-valence chromium species, which exhibited exceptional catalytic activity in various symbolic performance evaluations, such as propane dehydrogenation, toluene oxidation, and benzyl alcohol oxidation, at the unsaturated sites. The spatial distribution of complex coordination around chromium sites was determined using atomic deciphering combined with the pair distribution function and reverse Monte Carlo. This analysis confirmed that the unsaturated structure is preferentially assembled on the surface with a proportion of 83%. Analyzing the catalytic mechanism of $CrO_x$-based nanocatalysts is facilitated by parsing unsaturated active regions. This process also enhances our atomic understanding of oxide catalyst structures.

## ASSOCIATED CONTENT

### Supporting Information

The Supporting Information is available free of charge at https://pubs.acs.org/doi/10.1021/acs.chemmater.4c02260.



https://doi.org/10.1021/acs.chemmater.4c02260
Chem. Mater. XXXX, XXX, XXX−XXX

Equations for catalyst performance; chromium(III) nitrate nonahydrate decomposition stage estimation; characterization data including TEM images and size distribution histograms, XRD data, EPR data, XPS spectra, $H_2$-TPR, Cr K-edge XAFS data, PDF data, ICP, BET, and TG analysis for spent catalysts (PDF)

## AUTHOR INFORMATION


### Corresponding Author

**Qiang Li** − *Beijing Advanced Innovation Center for Materials Genome Engineering, Institute of Solid State Chemistry, University of Science and Technology Beijing, Beijing 100083, China;* orcid.org/0000-0003-4259-6984; Email: qiangli@ustb.edu.cn

### Authors

**Mingxin Lv** − *Beijing Advanced Innovation Center for Materials Genome Engineering, Institute of Solid State Chemistry, University of Science and Technology Beijing, Beijing 100083, China*

**Fan Xue** − *Beijing Advanced Innovation Center for Materials Genome Engineering, Institute of Solid State Chemistry, University of Science and Technology Beijing, Beijing 100083, China*

**Zhiguo Li** − *Beijing Advanced Innovation Center for Materials Genome Engineering, Institute of Solid State Chemistry, University of Science and Technology Beijing, Beijing 100083, China*

**Peixi Zhang** − *Beijing Advanced Innovation Center for Materials Genome Engineering, Institute of Solid State Chemistry, University of Science and Technology Beijing, Beijing 100083, China*

**Longlong Fan** − *Institute of High Energy Physics, CAS, Beijing 100049, China;* orcid.org/0000-0002-1748-1192

**Jianrong Zeng** − *Shanghai Synchrotron Radiation Facility, Shanghai Advanced Research Institute, Chinese Academy of Sciences, Shanghai 201204, China; Shanghai Institute of Applied Physics, Chinese Academy of Sciences, Shanghai 201800, China*

**Mengshi Li** − *State Key Laboratory of Chemical Resource Engineering, Beijing Engineering Center for Hierarchical Catalysts, Beijing University of Chemical Technology, Beijing 100029, China*

**Yufei He** − *State Key Laboratory of Chemical Resource Engineering, Beijing Engineering Center for Hierarchical Catalysts, Beijing University of Chemical Technology, Beijing 100029, China;* orcid.org/0000-0003-4487-9865

**Dianqing Li** − *State Key Laboratory of Chemical Resource Engineering, Beijing Engineering Center for Hierarchical Catalysts, Beijing University of Chemical Technology, Beijing 100029, China;* orcid.org/0000-0001-6761-8946

**Qiheng Li** − *Beijing Advanced Innovation Center for Materials Genome Engineering, Institute of Solid State Chemistry, University of Science and Technology Beijing, Beijing 100083, China*

**Xin Chen** − *Beijing Advanced Innovation Center for Materials Genome Engineering, Institute of Solid State Chemistry, University of Science and Technology Beijing, Beijing 100083, China*

**Kun Lin** − *Beijing Advanced Innovation Center for Materials Genome Engineering, Institute of Solid State Chemistry, University of Science and Technology Beijing, Beijing 100083, China;* orcid.org/0000-0003-4515-3206

**Jinxia Deng** − *Beijing Advanced Innovation Center for Materials Genome Engineering, Institute of Solid State Chemistry, University of Science and Technology Beijing, Beijing 100083, China*

**Xianran Xing** − *Beijing Advanced Innovation Center for Materials Genome Engineering, Institute of Solid State Chemistry, University of Science and Technology Beijing, Beijing 100083, China;* orcid.org/0000-0003-0704-8886

Complete contact information is available at: https://pubs.acs.org/10.1021/acs.chemmater.4c02260


### Notes

The authors declare no competing financial interest.

## ACKNOWLEDGMENTS

This research was supported by the National Key R&D Program of China (2020YFA0406202) and the National Natural Science Foundation of China (22090042 and 22175018). The total scattering experiments were performed at the beamline 3W1 of the Beijing Synchrotron Radiation Facility and BL13SSW beamline of the Shanghai Synchrotron Radiation Facility. X-ray absorption fine structure (XAFS) spectra were collected at the BL13SSW beamline of the Shanghai Synchrotron Radiation Facility.

## REFERENCES


(1) Guo, Z.; Liu, B.; Zhang, Q.; Deng, W.; Wang, Y.; Yang, Y. Recent advances in heterogeneous selective oxidation catalysis for sustainable chemistry. *Chem. Soc. Rev.* **2014**, *43* (10), 3480−3524.

(2) Chen, S.; Chang, X.; Sun, G.; Zhang, T.; Xu, Y.; Wang, Y.; Pei, C.; Gong, J. Propane dehydrogenation: catalyst development, new chemistry, and emerging technologies. *Chem. Soc. Rev.* **2021**, *50* (5), 3315−3354.

(3) Trummer, D.; Searles, K.; Algasov, A.; Guda, S. A.; Soldatov, A. V.; Ramanantoanina, H.; Safonova, O. V.; Guda, A. A.; Copéret, C. Deciphering the Phillips Catalyst by Orbital Analysis and Supervised Machine Learning from Cr Pre-edge XANES of Molecular Libraries. *J. Am. Chem. Soc.* **2021**, *143* (19), 7326−7341.

(4) Sinha, A. K.; Suzuki, K. Novel mesoporous chromium oxide for VOCs elimination. *Appl. Catal., B* **2007**, *70* (1−4), 417−422.

(5) Wang, J.; Song, Y.-H.; Liu, Z.-T.; Liu, Z.-W. Active and selective nature of supported CrOx for the oxidative dehydrogenation of propane with carbon dioxide. *Appl. Catal., B* **2021**, *297*, 120400.

(6) Grzybowska, B.; Słoczyński, J.; Grabowski, R.; Wcisło, K.; Kozłowska, A.; Stoch, J.; Zieliński, J. Chromium oxide/alumina catalysts in oxidative dehydrogenation of isobutane. *J. Catal.* **1998**, *178* (2), 687−700.

(7) Santhoshkumar, M.; Hammer, N.; Ronning, M.; Holmen, A.; Chen, D.; Walmsley, J.; Oye, G. The nature of active chromium species in Cr-catalysts for dehydrogenation of propane: New insights by a comprehensive spectroscopic study. *J. Catal.* **2009**, *261* (1), 116−128.

(8) Dera, P.; Lavina, B.; Meng, Y.; Prakapenka, V. B. Structural and electronic evolution of $Cr_2O_3$ on compression to 55 GPa. *J. Solid State Chem.* **2011**, *184* (11), 3040−3049.

(9) Moisii, C.; Deguns, E. W.; Lita, A.; Callahan, S. D.; van de Burgt, L. J.; Magana, D.; Stiegman, A. Coordination environment and vibrational spectroscopy of Cr (VI) sites supported on amorphous silica. *Chem. Mater.* **2006**, *18* (17), 3965−3975.

(10) Zhang, L.; Chen, K.; Chen, H.; Han, X.; Liu, C.; Qiao, L.; Wu, W.; Yang, B. Elucidating the promoting advantages and fundamentals for their creation in Sn-modified commercial CrOx/Al2O3 catalyst for propane dehydrogenation. *Chem. Eng. J.* **2024**, *483*, 149366.

(11) Shifa, T. A.; Gradone, A.; Yusupov, K.; Ibrahim, K. B.; Jugovac, M.; Sheverdyaeva, P. M.; Rosen, J.; Morandi, V.; Moras, P.; Vomiero,

A. Interfacing $CrO_x$ and CuS for synergistically enhanced water oxidation catalysis. *Chem. Eng. J.* **2023**, *453*, 139781.
(12) Zhang, B.; Wang, J.; Liu, G.; Weiss, C. M.; Liu, D.; Chen, Y.; Xia, L.; Zhou, P.; Gao, M.; Liu, Y.; Chen, J.; Yan, Y.; Shao, M.; Pan, H.; Sun, W. A strongly coupled Ru−$CrO_x$ cluster−cluster heterostructure for efficient alkaline hydrogen electrocatalysis. *Nat. Catal.* **2024**, *7* (4), 441−451.
(13) Wang, A.; Lin, B.; Zhang, H.; Engelhard, M. H.; Guo, Y.; Lu, G.; Peden, C. H. F.; Gao, F. Ambient temperature NO oxidation over Cr-based amorphous mixed oxide catalysts: effects from the second oxide components. *Catal. Sci. Technol.* **2017**, *7* (11), 2362−2370.
(14) Zhang, Z.; He, D.; Huang, Z.; He, S.; Lu, J.; Luo, Y. Flowing-Air-Induced Transformation to Promote the Dispersion of the $CrO_x$ Catalyst for Propane Dehydrogenation. *ACS Appl. Mater. Interfaces* **2021**, *13* (17), 19873−19883.
(15) Dou, S.; Xu, J.; Cui, X.; Liu, W.; Zhang, Z.; Deng, Y.; Hu, W.; Chen, Y. High-Temperature Shock Enabled Nanomanufacturing for Energy-Related Applications. *Adv. Energy Mater.* **2020**, *10* (33), 2001331.
(16) Yang, C.; Ko, B. H.; Hwang, S.; Liu, Z.; Yao, Y.; Luc, W.; Cui, M.; Malkani, A. S.; Li, T.; Wang, X.; et al. Overcoming immiscibility toward bimetallic catalyst library. *Sci. Adv.* **2020**, *6* (17), No. eaaz6844.
(17) Liu, C.; Shen, Y.; Zhang, J.; Li, G.; Zheng, X.; Han, X.; Xu, L.; Zhu, S.; Chen, Y.; Deng, Y.; et al. Multiple twin boundary-regulated metastable Pd for ethanol oxidation reaction. *Adv. Energy Mater.* **2022**, *12* (8), 2103505.
(18) Wang, J.; Zhu, M.-L.; Song, Y.-H.; Liu, Z.-T.; Wang, L.; Liu, Z.-W. Molecular-level investigation on supported CrOx catalyst for oxidative dehydrogenation of propane with carbon dioxide. *J. Catal.* **2022**, *409*, 87−97.
(19) Shao, H.; He, Q.; Wang, D.; Zhang, Y.; Jiang, T.; Guo, X. The active sites and catalytic properties of $CrO_x$/Zn-$Al_2O_3$ catalysts for propane dehydrogenation. *Appl. Catal., A* **2022**, *637*, 118610.
(20) Weckhuysen, B. M.; De Ridder, L. M.; Schoonheydt, R. A. A quantitative diffuse reflectance spectroscopy study of supported chromium catalysts. *J. Phys. Chem.* **1993**, *97* (18), 4756−4763.
(21) Weckhuysen, B. M.; Verberckmoes, A. A.; Buttiens, A. L.; Schoonheydt, R. A. Diffuse reflectance spectroscopy study of the thermal genesis and molecular structure of chromium-supported catalysts. *J. Phys. Chem.* **1994**, *98* (2), 579−584.
(22) Khaddar-Zine, S.; Ghorbel, A.; Naccache, C. EPR and UV−visible spectroscopic studies of alumina-supported chromium oxide catalysts. *J. Mol. Catal. A: Chem.* **1999**, *150* (1−2), 223−231.
(23) Dines, T. J.; Inglis, S. Raman spectroscopic study of supported chromium(vi) oxide catalysts. *Phys. Chem. Chem. Phys.* **2003**, *5* (6), 1320−1328.
(24) Moisii, C.; Jeffcoat, D.; Peek, N.; van de Burgt, L.; Scott, S. L.; Stiegman, A. E. Do Mono-oxo Sites Exist in Silica-Supported Cr(VI) Materials? Reassessment of the Resonance Raman Spectra. *J. Phys. Chem. C* **2018**, *122* (30), 17149−17160.
(25) Ravel, B.; Newville, M. ATHENA , ARTEMIS , HEPHAESTUS: data analysis for X-ray absorption spectroscopy using IFEFFIT. *J. Synchro. Radiat.* **2005**, *12* (4), 537−541.
(26) Funke, H.; Scheinost, A. C.; Chukalina, M. Wavelet analysis of extended x-ray absorption fine structure data. *Phys. Rev. B* **2005**, *71*, 094110.
(27) Qiu, X.; Thompson, J. W.; Billinge, S. J. PDFgetX2: a GUI-driven program to obtain the pair distribution function from X-ray powder diffraction data. *J. Appl. Crystallogr.* **2004**, *37* (4), 678−678.
(28) Tucker, M.; Dove, M.; Goodwin, A.; Phillips, A.; Keen, D.; Playford, H.; Slawinski, W. A.; Levin, I.; Krayzman, V.; Eremenko, M.et al.*RMCProfile User Manual Code Version 6.7.4*RMCProfile2019
(29) Melnikov, P.; Nascimento, V.; Arkhangelsky, I.; Zanoni Consolo, L.; De Oliveira, L. Thermolysis mechanism of chromium nitrate nonahydrate and computerized modeling of intermediate products. *J. Therm. Anal. Calorim.* **2013**, *114*, 1021−1027.
(30) Cavani, F.; Koutyrev, M.; Trifiro, F.; Bartolini, A.; Ghisletti, D.; Iezzi, R.; Santucci, A.; Del Piero, G. Chemical and physical characterization of alumina-supported chromia-based catalysts and their activity in dehydrogenation of isobutane. *J. Catal.* **1996**, *158* (1), 236−250.
(31) Michorczyk, P.; Ogonowski, J.; Kuśtrowski, P.; Chmielarz, L. Chromium oxide supported on MCM-41 as a highly active and selective catalyst for dehydrogenation of propane with $CO_2$. *Appl. Catal., A* **2008**, *349* (1−2), 62−69.
(32) Chakrabarti, A.; Wachs, I. E. The nature of surface $CrO_x$ sites on $SiO_2$ in different environments. *Catal. Lett.* **2015**, *145*, 985−994.
(33) Weckhuysen, B. M.; Wachs, I. E.; Schoonheydt, R. A. Surface chemistry and spectroscopy of chromium in inorganic oxides. *Chem. Rev.* **1996**, *96* (8), 3327−3350.
(34) Weckhuysen, B. M.; Schoonheydt, R. A.; Mabbs, F. E.; Collison, D. Electron paramagnetic resonance of heterogeneous chromium catalysts. *J. Chem. Soc., Faraday Trans.* **1996**, *92* (13), 2431−2436.
(35) Su, J.; Yao, W.; Liu, Y.; Wu, Z. The impact of CrOx loading on reaction behaviors of dichloromethane (DCM) catalytic combustion over Cr-O/HZSM-5 catalysts. *Appl. Surf. Sci.* **2017**, *396*, 1026−1033.
(36) Szulczewski, M. D.; Helmke, P. A.; Bleam, W. F. Comparison of XANES analyses and extractions to determine chromium speciation in contaminated soils. *Environ. Sci. Technol.* **1997**, *31* (10), 2954−2959.
(37) Peterson, M. L.; Brown Jr, G. E.; Parks, G. A.; Stein, C. L. Differential redox and sorption of Cr (III/VI) on natural silicate and oxide minerals: EXAFS and XANES results. *Geochim. Cosmochim. Acta* **1997**, *61* (16), 3399−3412.
(38) Conley, M. P.; Delley, M. F.; Núñez-Zarur, F.; Comas-Vives, A.; Copéret, C. Heterolytic Activation of C−H Bonds on CrIII−O Surface Sites Is a Key Step in Catalytic Polymerization of Ethylene and Dehydrogenation of Propane. *Inorg. Chem.* **2015**, *54* (11), 5065−5078.
(39) Sattler, J. J.; Ruiz-Martinez, J.; Santillan-Jimenez, E.; Weckhuysen, B. M. Catalytic dehydrogenation of light alkanes on metals and metal oxides. *Chem. Rev.* **2014**, *114* (20), 10613−10653.
(40) Zhu, H.; Yang, C.; Li, Q.; Ren, Y.; Neuefeind, J. C.; Gu, L.; Liu, H.; Fan, L.; Chen, J.; Deng, J.; et al. Charge transfer drives anomalous phase transition in ceria. *Nat. Commun.* **2018**, *9* (1), 5063.
(41) Li, Q.; Zhu, H.; Chen, X.; Liu, H.; Ren, Y.; Chen, Y.; Ohara, K.; Zhou, L.; Chen, J.; Deng, J.; et al. Local structure insight into hydrogen evolution reaction with bimetal nanocatalysts. *J. Am. Chem. Soc.* **2022**, *144* (44), 20298−20305.
(42) Fang, H.; Wang, W.; Jablonski, P. D.; Liu, Z. Effects of reactive elements on the structure and diffusivity of liquid chromia: An ab initio molecular dynamics study. *Phys. Rev. B: Condens. Matter Mater. Phys.* **2012**, *85* (1), 014207.
(43) Stephens, J.; Cruickshank, D. The crystal structure of (CrO3)∞. *Acta Cryst. B* **1970**, *26* (3), 222−226.
(44) Baek, J.; Yun, H. J.; Yun, D.; Choi, Y.; Yi, J. Preparation of Highly Dispersed Chromium Oxide Catalysts Supported on Mesoporous Silica for the Oxidative Dehydrogenation of Propane Using $CO_2$: Insight into the Nature of Catalytically Active Chromium Sites. *ACS Cata.l* **2012**, *2* (9), 1893−1903.
(45) Fridman, V. Z.; Xing, R.; Severance, M. Investigating the $CrO_x$/$Al_2O_3$ dehydrogenation catalyst model: I. identification and stability evaluation of the Cr species on the fresh and equilibrated catalysts. *Appl. Catal., A* **2016**, *523*, 39−53.
(46) Delley, M. F.; Silaghi, M.-C.; Nuñez-Zarur, F.; Kovtunov, K. V.; Salnikov, O. G.; Estes, D. P.; Koptyug, I. V.; Comas-Vives, A.; Copéret, C. X−H Bond activation on Cr (III), O sites (X= R, H): Key steps in dehydrogenation and hydrogenation processes. *Organomet* **2017**, *36* (1), 234−244.


https://doi.org/10.1021/acs.chemmater.4c02260
Chem. Mater. XXXX, XXX, XXX−XXX